PNAS
www.pnas.org

Supplementary Information for

Intrinsically Ultrastrong Plasmon-Exciton Interactions in Crystalline Films of Carbon Nanotubes

Po-Hsun Ho, Damon B. Farmer, George S. Tulevski, Shu-Jen Han, Douglas M. Bishop, Lynne M. Gignac, Jim Bucchignano, Phaedon Avouris, Abram L. Falk

Abram L. Falk
Email: alfalk@us.ibm.com

Phaedon Avouris
Email: phaedon.avouris@gmail.com

This PDF file includes:

www.pnas.org/cgi/doi/10.1073/pnas.1816251115

S1. Properties of the nanotube suspension

To verify that the nanotubes are indeed well dispersed in SDBS suspension, we have checked this suspension by drop-casting it on blank silicon chips, drying the chips, and imaging them with atomic force microscopy. No nanotubes whose height is greater than 2 nm are observed (Fig. S1), indicating that our sonication and centrifugation processes are effective at removing bundles from the suspension.

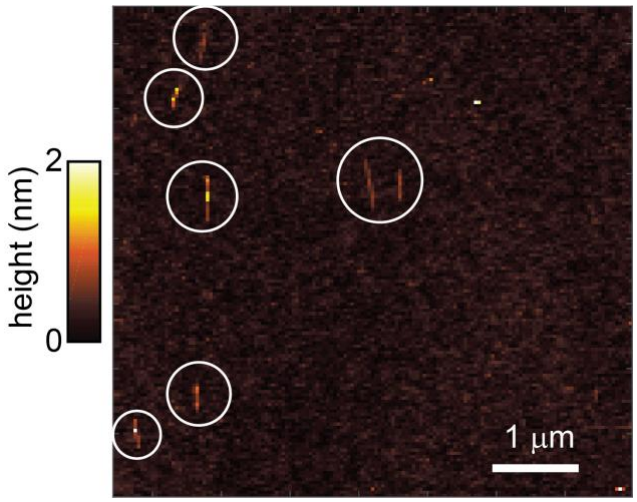

Fig. S1. Atomic force microscopy (AFM) image of nanotubes that are drop-casted and dried on a silicon chip. They are from an aqueous SDBS suspension that was used to fabricate our crystallized nanotube films.

S2. Crystal structure of the nanotube films

With the modified vacuum filtration method, a one-inch crystalline nanotube film was deposited on a polycarbonate membrane (Fig. S2). As discussed in SI Ref. (1), this process can potentially be readily extend to the wafer scale by using a larger fritted glass and membrane. Both the microscopic and macroscopic crystalline properties of this nantoube film were measured by selective area electron diffraction and grazing-incidence X-ray diffraction.

Fig. S3*A* shows a cross-sectional TEM image of a crystalline nanotube film. We measured the selective area diffraction pattern in regions of this image (Fig. S3*A*). The corresponding diffraction patterns are shown in Fig. S3*B*. Different crystal angles of hexagonal lattice were observed, indicating that this nanotube film is polycrystalline.

Grazing incidence X-ray diffraction (XRD) was used to further characterize the crystallinity of the aligned CNT arrays. The reason that the grazing incidence mode was chosen is that it is particularly effective at measuring thin films. Here, we focus on the low angle diffraction related to the >1 nm lattice constant from the lattice of nanotube (as opposed to the much higher angle diffraction coming from the carbon lattices of the comprising nanotubes).

The XRD was performed with a Siemens D5000 XRD spectrometer and a Cu-Kα (λ = 1.54 Å) x-ray source. The incident angle was fixed at 2.2°, and the angle of the detector was swept. A strong discrete peak is observed at 2 = 5.8°, which corresponds with the lattice spacing of the aligned nanotube arrays. Based on the two-dimensional hexagonal lattice of nanotubes indicated by the selected area TEM diffraction (Fig. 1*C*, 1*D*, and Fig. S3*B*), this signal comes from the (10) plane of the lattice. The $d_{(10)}/a$ ratio is $\sqrt{3/2}$, where a is the lattice constant. Bragg's law, $2d \sin\theta = n\lambda$, therefore indicates that the lattice constant of the nanotube lattice is a = 1.74 nm. In light of the D = 1.41 nm average diameter of nanotubes, as specified by the nanotube manufacturer, the van der Waals gap between neighboring nanotubes, a - D, is 3.3 Å.

XRD measurements with the nanotube sample oriented in different directions relative to the incident light were also performed (Fig. S4*A*). The collected data are all indexed and shown in Fig. S4*B*. When the CNTs are parallel to the incident plane, the strongest (10) and (11) signals were obtained. However, the higher index signals were smaller than those corresponding to other alignment directions. These results confirm the preferred orientation direction of the polycrystalline CNT film.

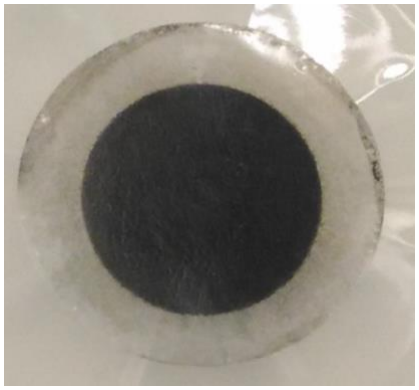

Fig. S2. A photograph of a 1-inch-in-diameter CNT film on a membrane.

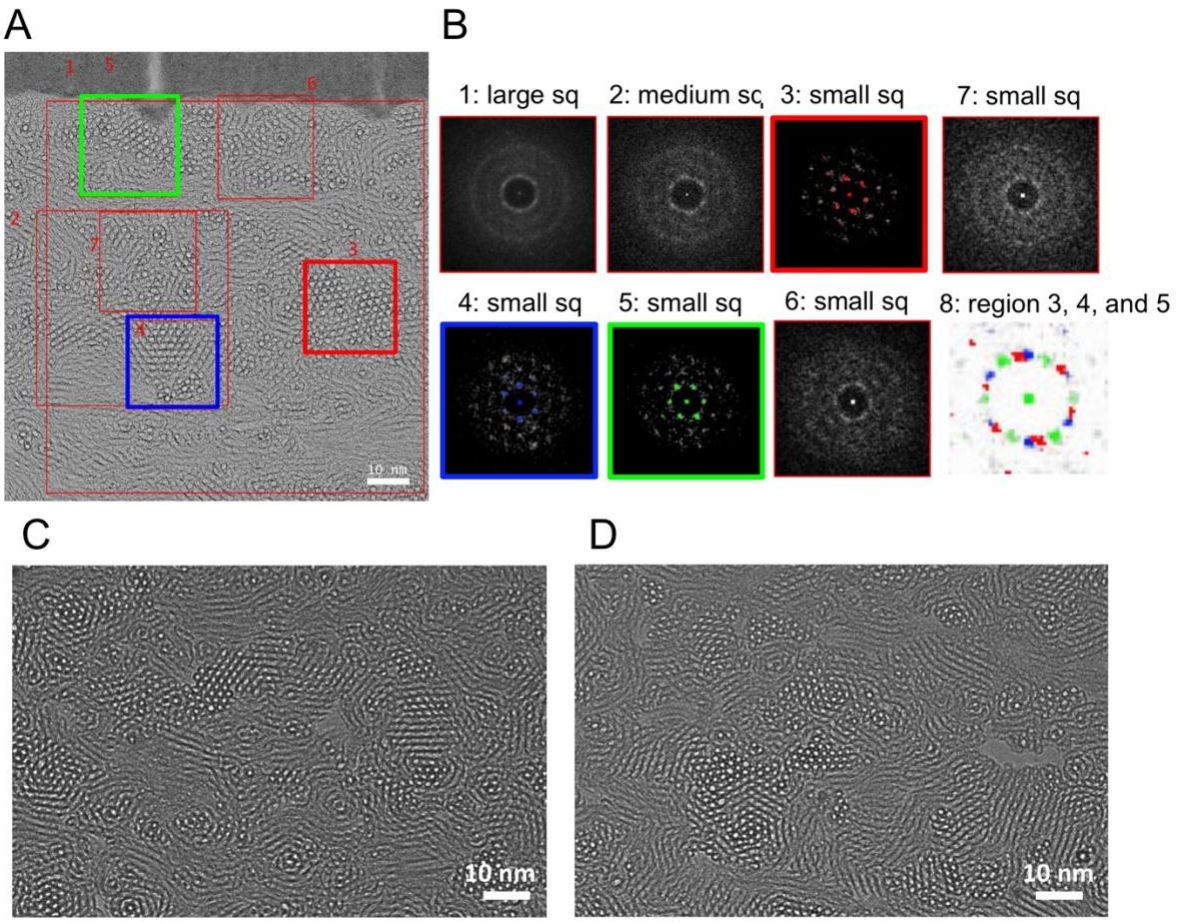

Fig. S3. (*A*) A cross-sectional TEM image of the nanotube film shown in Figs. 1*A*-*C*. **(***B*) Selective area electron diffraction patterns (SAED), corresponding to the regions marked in Fig. S3*A*. In image #8, the locations of the diffraction spots regions 3, 4, and 5 are combined. **(***C*) and **(***D*) Cross-sectional TEM images of another nanotube film, also showing clear polycrystallinity.

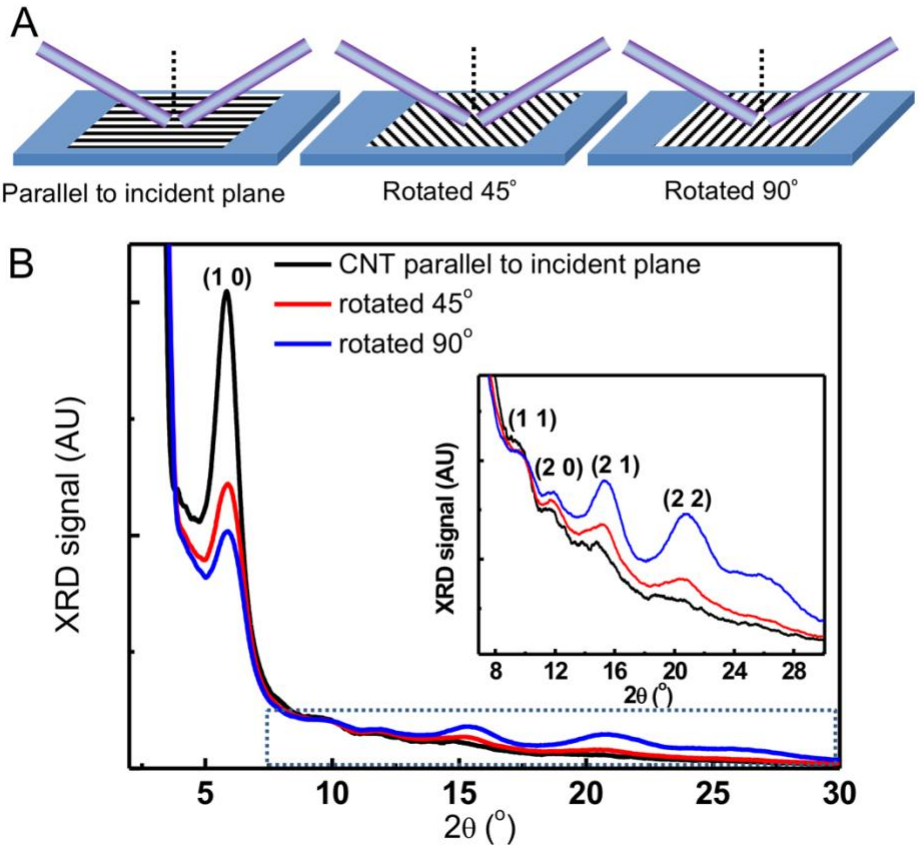

Fig. S4. Angle-dependent XRD measurements. (*A*) Schematic images of XRD measurements with different orientations of the CNT film (the black lines) relative to the x-ray beam. (*B*) XRD profile of the CNT film with different orientations. Inset: magnified image of the high angle region (dashed box in the main figure panel).

S3. Spectroscopy methods

The extinction spectra were measured in a Bruker Nicolet 8700 μ-FTIR system. The diameter of the focused beam size is 100 μm, and each measurement was integrated for a 100-second period. Before each spectrum is taken, a background spectrum is taken, on an area of the chip in which the carbon nanotubes have been completely etched away. The spectrometer outputs absorbance relative to the background spectrum. The extinction is then calculated as

$$Extinction = 1 - 10^{-absorbance(\nu)}. \qquad [S1]$$

Measurements of the high frequency plasmon resonances in thick films ($\hbar\omega_p$ > 0.85 eV, see Fig. 4*A*), which were out of the range of our FTIR system, were executed using a PerkinElmer Lambda 950 UV-VIS-NIR spectrometer. The films we prepared for use in this system were similar to the ones that we prepared for FTIR, except 1) larger patterns (3 mm × 7 mm) were prepared, to accommodate the larger beam size of this spectrometer, and 2) sapphire substrates were used instead of silicon, to extend the range to higher energies.

Fig. S5 presents the non-normalized (i.e. as-measured) extinction spectra corresponding to Figs. 2*C* and 2*D*. In both spectra, we observe that as the lithographically defined CNT length (*L*) becomes shorter, the extinction signal becomes less, even though a 1:1 nanotube:gap coverage ratio is maintained. The simplest explanation for this phenomenon is that, as *L* is reduced, there is an increasing wavevector mismatch between the nanotube resonators and free space. Another contributing factor may be damaged ends of the nanotubes, which arise from the reactive ion etching, reducing the absorption of the shorter-*L* nanotubes.

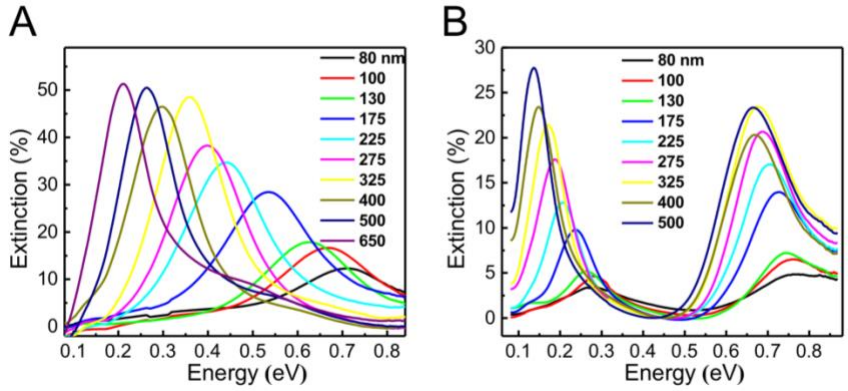

Fig. S5. Extinction spectra without normalization. (*A*) The nanotube resonators are in a high doping-level state. The film thickness is t = 49 nm. The etched nanotube length (*L*) is given in the legend. (*B*) The nanotube resonators are in a low doping-level (annealed) state. In Figs. 3*B*-*C* of the main text, we normalized the height of the extinction spectra and offset them from each other, for clarity of presentation. Here, we present the same data, except that we do not normalize the curves or offset them from one another.

S4. Optical transitions of the crystalline nanotube films

We used an FTIR spectrometer to perform all of the extinction spectroscopy measurements in the main text. However, this instrument only measures energies up to 0.95 eV. To measure higher energy optical transitions in our crystalline nanotube films, we used a PerkinElmer Lambda 950 UV-VIS-NIR spectrometer. For these measurements, to avoid silicon absorption, we used sapphire substrates. The detection area of this system is 25 mm^2.

Figure S6 presents the UV-VIS spectra of a 20 nm-thick film with different doping levels. Three excitons can be clearly identified: the S_{11} and S_{22} excitons of semiconducting CNTs, and the M_{11} exciton of metallic CNTs. With increasing *p*-type free charge density, the S_{11} excitons are quenched first, due to depopulation of the highest-energy valence states. The S_{22} exciton is next to be quenched. At very high doping levels, the selection rules of the optical transitions are modified, allowing new inter-valance-band transitions (2). Therefore, new optical transitions can be observed. In our CNT film, we observe an inter-valence band transition S_{41}, whose energy is 1.04 eV. This state has previously been observed in strongly doped CNT films (2, 3). These inter-valance excitons persist at high *p*-type doping levels and can strongly couple to plasmon resonances. They are likely responsible for the saturating resonance energies at 0.9 eV that are observed in Fig. 4*D* of the main text.

The strength of the interband excitons and the plasmon resonances have opposed doping dependences. Because plasmons comprise charge oscillations, the plasmon resonance strengthens as the doping level increases and more free charges are available. On the other hand, an increase in the doping level causes a depopulation of the band-edge states that leads to a smaller density of available transitions for interband nanotube excitons. Thus, the exciton transition strength decreases with increasing doping level.

Nonetheless, there is a substantial regime of moderate doping levels in which the exciton and the plasmon resonance are both strong. As Fig. S6 and S7 show, while the S_{11} exciton is eventually quenched at high doping levels, it persists and is reasonably strong at a variety of moderate

doping levels. This persistence is confirmed by absorption measurements in previous studies (2, 3), as well as two-photon fluorescence studies of nanotube exciton binding energies (4) that are performed in ambient conditions, where nanotubes are doped by surface adsorbates.

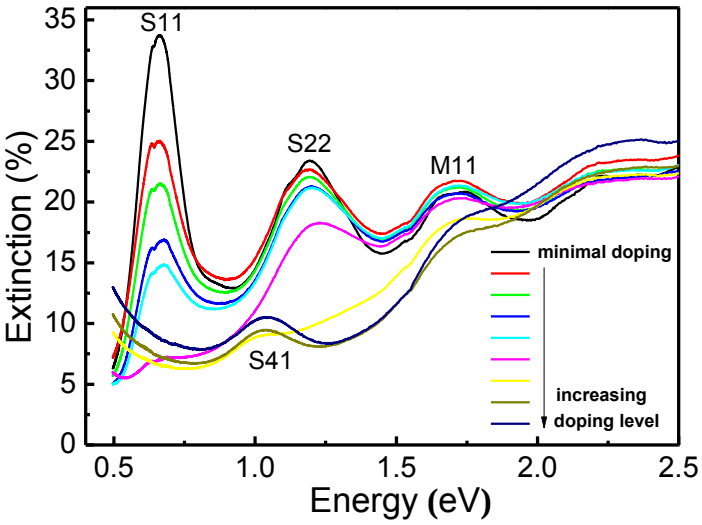

Fig. S6. UV-VIS extinction spectra of an unpatterned 20-nm-thick crystallized nanotube film, as a function of chemically induced charge-carrier density. Although S_{11} and S_{22} decrease in intensity with increasing doping level, a new peak, S_{41}, emerges at very high doping levels (2, 3).

As for the plasmon resonance, although it strongly redshifts with lower doping levels, it remains reasonably strong at all doping levels that we can access, even in the "annealed, resistive" state of our patterned films, which is the state of our films in Figs. 3*C-D* and Fig. 4*C*. We note that the conductivity in this state is only 30 times lower than that of the most strongly doped state – a much lower on/off ratio than that of a pure semiconducting nanotube or a film of purely semiconducting nanotubes.

Figure S7 shows the coexistence of the plasmon and exciton resonances in a patterned crystallized nanotube film. In this film, t = 49 nm and L = 650 nm. The long L value is chosen so that $\omega_p << \omega_0$, and thus, the plasmons and excitons are not hybridized.

For the highest doping level (the turquoise curve), which is the state of the film immediately after HNO_3 vapor exposure, the S_{11} exciton transition strength at ω_0 is quenched. Here, there is only a single extinction peak, which corresponds to the plasmon resonance. However, at the four lower doping levels, the exciton and plasmon can be seen to coexist. For the three lowest doping levels, extinction from both the exciton and plasmon can be seen to be strong.

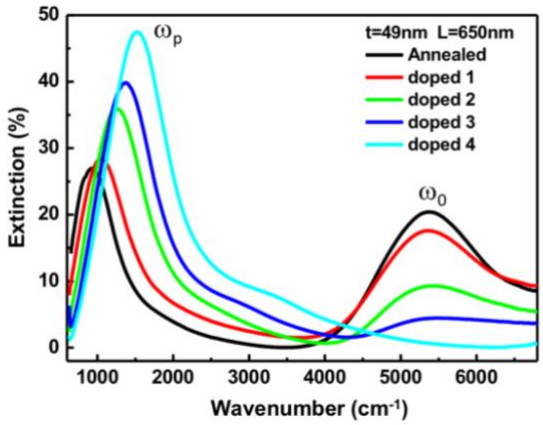

Fig. S7. FTIR extinction spectra of nanotube resonators with varying doping densities. The film is patterned into resonators (see Fig. 2) with L = 650 nm. With this long L-value, the plasmons and excitons are uncoupled. This figure shows that there is a substantial doping regime in which both strong plasmon resonances and strong exciton absorption can both be present.

S5. Resistivity of the crystalline nanotube films

An in-line four probe method was used to measure the resistivity of our crystallized CNT films. For a film of thickness t = 100 nm, in its minimal doping state (i.e. measured right after it has been annealed in vacuum), the as-measured four-probe resistance is R_x = 171 Ω, where R_x corresponds to the resistance in the nanotube alignment axis. The four-probe resistance measured perpendicular to the alignment axis (R_y) is four times higher than R_x. After the nanotube films are exposed to HNO_3 vapor, when the nanotube films are in a highly chemically doped state, R_x is reduced by a factor of 30.

To calculate the sheet resistivity, we model the CNT film as an infinite 2D sheet, and calculate the resistivity of nanotube film as $\rho_x = \frac{\pi}{\ln(2)} R_x t$. Using this formula, we calculate on-axis sheet resistivities of 7.6×10^{-3} Ω·cm (after vacuum annealing) and 2.6×10^{-4} Ω·cm (after HNO_3 vapor treatment). We note that, due to the anisotropy of the film, the factor of $\frac{\pi}{\ln 2}$, which accounts for the spread of current in the sheet, overestimates the true current spread in our film. The resistivities that we report should thus be understood as conservative estimates that modestly overestimate the true resistivity of our films.

S6. Linear dichroism of the nanotube resonators

Figure S8 shows the exctinction spectra of a film of plasmon resonators as a function of incident light polarization. The peak absorption is 20%, when the incident light polarization is parallel to the nanotube alignment axis, vs. approximately 0.15%, when the light is perpendicular to it. Accordingly, we calculate the degree of linear dichroism of the nanotube resonators to be 99%.

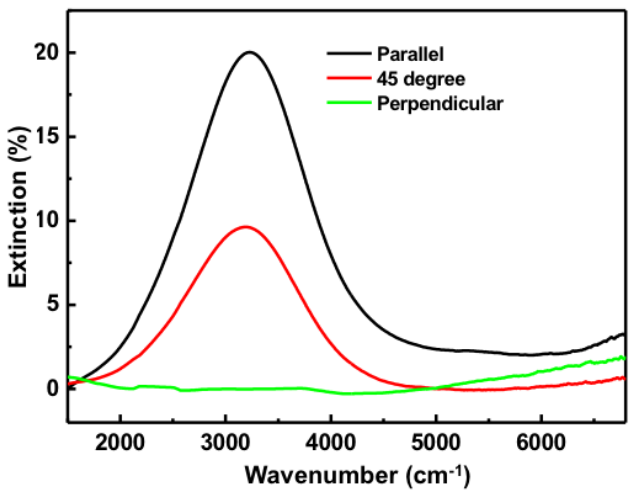

Fig. S8. Linear dichroism of the plasmon resonators. Polarization-dependent extinction data of plasmon resonators comprising an etched crystallized nanotube film with t = 49 nm and L = 130 nm. The nanotubes are in a highly doped state. The polarization of light is varied from being parallel (black curve), 45° (red curve), and perpendicular to the nanotube alignment axis.

S7. Quasi-2D dispersion of the nanotube nanoribbons

As mentioned in the main text, in the heavily doped state, the plasmon resonance energy of our nanotube nanoribbons follows a $\omega_p \propto \sqrt{tq}$ dependence, where t is the nanotube film thickness (see Fig. 2) and $q = \pi/L$, until $\hbar\omega_p$ saturates at 0.9 eV (see Fig. 4*D*). We previously experimentally verified this relationship (5), and one can also see the $\sqrt{q}$ relationship in Fig. 3*D*.

This $\omega_p \propto \sqrt{tq}$ relationship follows from the quasi-2D nature of the nanotube nanoribbons. The $\sqrt{q}$ dependence is also observed in graphene nanoribbons (6), and the t-dependence follows from the fact that the sheet-charge density in the nanoribbons is proportional to the film thickness.

Intuitively, the $\sqrt{q}$ dependence can be understood from Fig. S9. In the quasi-2D picture, the plasmon oscillation conists of 1D lines of charges that oscillate parallel to the nanotube alignment axis. From Gauss's law, the attractive electric force between the positive and negative lines of charge, at their maximum separation of L, is proportional to $1/L$. As a simple harmonic oscillator, the resonance frequence of this oscillationnanoribbon has a resonance frequency that is proportional to the square root of this force. Thus, $\omega \propto \sqrt{q}$.

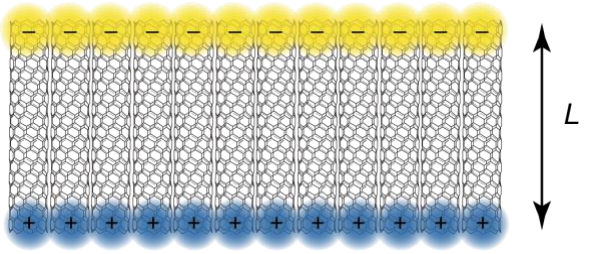

Fig. S9. After being etched into nanoribbons, our nanotube films form resonators with a quasi-2D dispersion relationship.

S8. Variation of the spacing between nanotube plasmon resonators

For all of the data in the main text of this manuscript, the ratio of the etched length of the nanotubes (L) and the spacing between them (s) is kept fixed at 1:1. Here, in Fig. S10, we show data in which s is varied from 130 to 325 nm, while L is kept constant at 325 nm. As s is decreased, the total absorption in both the exciton and plasmon resonances goes up, a simple consequences of the higher nanotube coverage in the measurement area. However, the center resonance frequency of neither peak changes substantially with s. This can be understood as a consequence of the fact that even s = 130 nm, the minimum spacing that we could achieve with our oxygen plasma etcher, is a much larger spacing than the inter-nanotube spacing within the crystallized films (1.74 nm). Thus, although our fabricated structures are large gratings of nanotube nanoribbons in order to fill up the measurement area of our FTIR spectrometer, each nanoribbon can be approximately understood as an isolated entity.

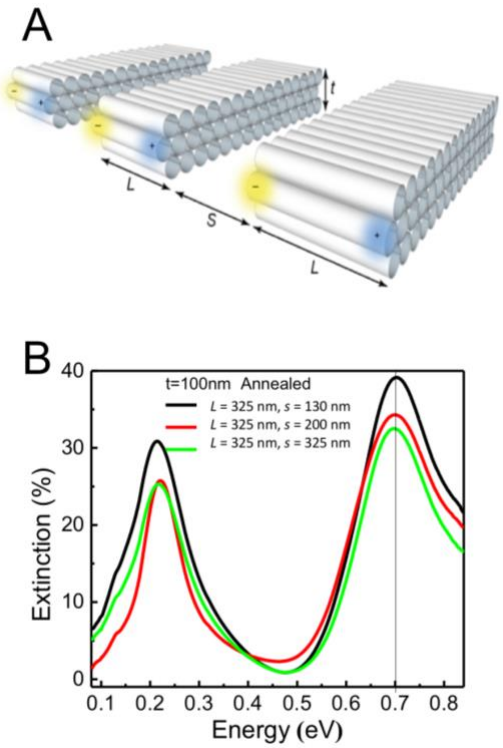

Fig. S10. Variation of the spacing between nanotube plasmon resonators. (*A*) Cartoon of the nanotube resonators showing the parameters *L* and *s*. (*B*) Extinction spectra of the nanotube resonators, in a low-doping-level state, with *L* fixed at 325, and *s* varied.

S9. Association between upper and lower plasmon-exciton polariton branches

The plasmon-exciton Rabi splitting is extremely large in our system. As a result, the fact that the plasmon and exciton branches are truly anticrossing, and not independently evolving with *L*, is important to establish. In this section, we provide a supplementary discussion of the evidence indicating that the apparent anticrossing truly derives from plasmon-exciton coupling, and not from an independent evolution of plasmons and excitons that mimics this coupling.

1. Evolution of ω_+ with *L* is only seen when ω_p is sufficiently high.

We observe that the frequency of the higher energy peak only deviates from being a constant ω_0 when ω_p approaches ω_0. In this case, the excitons and plasmons are hybridized, and the lower/higher energy peaks are respectively the ω_-/ω_+ polaritons. When ω_p is much less than ω_0, then the excitons and plasmons are not hybridized. In this case, the lower energy peak is just ω_p , and the higher energy peak is ω_0, which stays nearly constant with respect to *q*. For

sufficiently small L, ω_p will eventually be high enough such that ω_p and ω_0 strongly couple. However, for thin films, this L value is much smaller (i.e. the corresponding q value is much higher).

This can be seen in Fig. 4*C* of the main text. Consider the different peak energies of the thinnest film (the t = 15 nm film) and the thickest film (the t = 200 nm film) at the q = 13 μm^{-1} point. For the thin film, the lower energy peak is at 0.12 eV which is 0.17 eV, significantly less than both ω_0 and $\omega_0 - \Omega$. The higher energy peak is at 0.67 eV, which is just 1.5% higher than ω_0 = 0.66 eV. This small degree of departure of the higher energy peak from ω_0 can be understood to result from the fact that the plasmons and excitons are not signficantly hybridized at the q = 13 μm^{-1} point for this thin film.

On the other hand, for a thick, t = 200 nm film, the excitons and plasmons are significantly hybridized at this q = 13 μm^{-1} point. Here, the polariton energies are $\hbar\omega_-$ = 0.28 eV and $\hbar\omega_+$ = 0.79 eV, which is 20% higher than ω_0. The deviation of ω_+ from ω_0 is 10 times stronger than that observed in the thin t = 15 nm film at q = 13 μm^{-1}. This high degree of $\hbar\omega_+$ evolution results from the hybridization of plasmons and excitons.

2. Existing literature has found that, absent cavity coupling, nanotube exciton energies are a constant function of nanotube length.

When plasmons are not coupled to the S_{11} exciton, the S_{11} exciton energy has been observed not to change with L (7). More specifically, in the range of nanotube lengths from 10 nm to 750 nm, Ref S4 finds no discernible change at all in the S_{11} energy.

3. In predominantly metallic nanotube resonators, the exciton energy does not evolve with L.

In addition to the films of with mixed-chirality nanotubes (2:1 semiconducting:metallic types) fabricated in the main text, we also fabricated films of aligned carbon nanotubes out of purified metallic nanotubes. We estimate that the residual fraction of semiconducting nanotubes in these films is S = 2 to 3%. We purchased these purified nanotubes from Nanointegris, Inc.,

and fabricated aligned films of metallic nanotubes films in a very similar manner to the films produced in the main text. We then etched these films into gratings and measured the peak energies, much as we did for the films in the main text.

Figure S11 shows the results. As with the S = 2/3 films studied in the main text, there is an upper and lower energy peak at each q value. However, for the S = 2-3% films, unlike the S = 2/3 main-text films films, the upper peak remains constant (ω_0) and does not evolve with L. This phenomenon can be understood to derive from the fact that the upper energy peak is nearly a pure exciton, not a plasmon-exciton polariton, because the concentration of semiconducting nanotubes is too low.

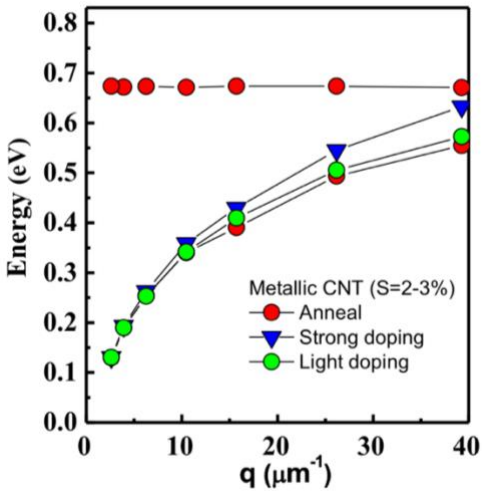

Fig. S11. Plasmons and excitons in films of nearly purely metallic nanotubes. The plot shows the two extinction peaks (the S_{11} exciton at 0.67 eV, and the plasmon resonance) of plasmon resonators etched into a t = 55 nm film of nanotubes, which are 97-98% metallic and 2-3% semiconducting. The S_{11} exciton, which is only strong enough to be observed when the nanotubes are in their most resistive state, has a constant (± 2%) energy with respect to q.

4. In thick nanotube films, the lower polariton has a flat shape, characteristic of strong coupling.

As discussed in Supplementary Information section S7, the energy of the nanotube plasmon resonances follows a $\omega_p \propto \sqrt{q}$ relationship. In contrast, for the thick nanotube films, where plasmon-exciton hybridization happens at low q values, the shape of ω_- clearly deviates from $\sqrt{q}$ and instead, has a flat, saturating shape. For instance, for the t = 250 nm film in Fig. 4*C*, the ω_- polariton is nearly completely flat by q = 10 μm^{-1}. This flat shape is a signature of strong coupling.

5. The Rabi splitting can be systematically controlled with doping level and thickness.

As expected from strong plasmon-exciton interactions, thickness and doping level are both parameters that can control Ω (see Fig. 4*B*). Naturally, at smaller Ω values, the fact that ω_- and ω_+ are anticrossing and not independently evolving becomes more apparent. In Fig. S12, in order to make Ω as small as we practically can, without quenching the S_{11} exciton with excessive free charge, we use a thick film (t = 200 nm) in a moderately doped state.

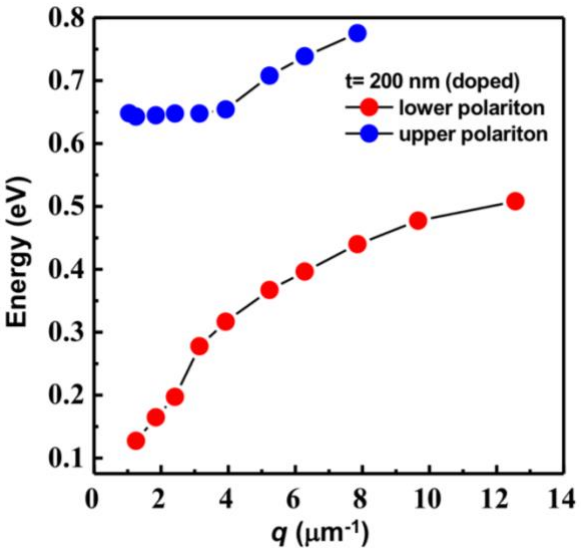

Fig. S12. Plasmon-exciton polaritons with a relatively small Ω in a thick, moderately doped film. To achieve a moderate doping level in this sample, it was exposed to HNO_3 vapor and then briefly annealed on a hot plate, so that $\sigma/\sigma_0 = 5$.

S10. References

1. He X, et al. (2016) Wafer-scale monodomain films of spontaneously aligned single-walled carbon nanotubes. *Nat Nanotechnol* 11(7):633–638.

2. Kim KK, et al. (2008) Fermi Level Engineering of Single-Walled Carbon Nanotubes by AuCl3 Doping. *J Am Chem Soc* 130(38):12757–12761.

3. Shin DW, et al. (2009) A role of HNO3 on transparent conducting film with single-walled carbon nanotubes. *Nanotechnology* 20(47):475703.

4. Wang F (2011) The Optical Resonances in Carbon Nanotubes Arise from Excitons. *Science*, 308(2005):838–841.

5. Chiu KC, et al. (2017) Strong and Broadly Tunable Plasmon Resonances in Thick Films of Aligned Carbon Nanotubes. *Nano Lett* 17(9):5641–5645.

6. Yan H, et al. (2013) Damping pathways of mid-infrared plasmons in graphene nanostructures. *Nat Photonics* 7(5):394–399.

7. Fagan JA, et al. (2007) Length-dependent optical effects in single-wall carbon nanotubes. *J Am Chem Soc* 129(34):10607–10612.